Engineering Geology 284 (2021) 106049

Contents lists available at ScienceDirect

Engineering Geology

journal homepage: www.elsevier.com/locate/enggeo

Temperature effect on gypsum-bearing soil and supported (building) foundations: The case of the Central Storage Facility of Villar de Cañas, Spain

Juan Alonso [a,*], Marina Moya [a], Vicente Navarro [b], Laura Asensio [b], José Antonio Aguado [c]

[a] Geoenvironmental Engineering Group, Universidad de Castilla - La Mancha, Campus Tecnológico de la Fábrica de Armas, Edificio 21, Avenida Carlos III s/n, Toledo, Spain

[b] Geoenvironmental Engineering Group, Universidad de Castilla - La Mancha, Avda. Camilo José Cela s/n, 13071, Ciudad Real, Spain

[c] Escuela de Arquitectura, Universidad de Castilla - La Mancha, Campus Tecnológico de la Fábrica de Armas, Edificio 21, Avenida Carlos III s/n, Toledo, Spain

ARTICLE INFO

Keywords:
Ground settlement
Thermo-hydro-mechanical modeling
Environmental geochemistry
Thermal load
Gypsum

ABSTRACT

Thermal load imposed on the ground by the foundations of some singular buildings may produce variations in geochemistry conditions. In soils containing soluble salts, such as gypsum, their dissolution/precipitation rates may be modified, triggering ground settlement as well as angular distortion of building foundations. This paper examines these processes for the case of the Central Storage Facility for high-level radioactive waste planned in Spain. This facility would impose a thermal load over a long period of time due to the disposal of spent nuclear fuel. A numerical model, including the equations for describing the dissolution/precipitation process, as well as the hydrogeological, thermal, chemical, and geomechanical changes in the ground caused by the construction and operation of the facilities, is proposed. The model focuses on the response of the building foundation under different hypothesis of thermal loading underneath the building. Comsol Multiphysics software was used for solving the resulting partial differential equations by the finite element method. This analysis concludes that moderate thermal loading of the ground would develop in the Case Study, with negligible mechanical effect on the foundation.

1. Introduction

The effects of dissolution or precipitation of gypsum and other soluble salts in soils beneath building foundations or civil engineering works have been broadly studied. This way, many authors have developed measures to protect structures from subsidence related to sinkhole activity (Gutiérrez et al., 2014; Paukštysa et al., 1999), dealt with damage to civil engineering works due to the degradation and swelling of clayey rocks bearing calcium sulfate (Oldecop and Alonso, 2012), or developed stabilizing techniques for problematic gypsiferous soils (Gumusoglu and Ulker, 1982; Kuttah and Sato, 2015). The relevance of these issues is linked to the rates at which dissolution processes occur. According to White (1984), the acceleration of dissolution and subsidence processes depends on a hydrodynamic and a chemical component. The former derives from changes in the local hydrogeology, such as the modification of the phreatic level or the path and rate of groundwater flow (Cooper and Gutiérrez, 2013). The second derives from changes in the chemical composition of the groundwater and the solubility product value, which in turn depends on the pressure and temperature conditions (Blount and Dickson, 1973; Freyer and Voigt, 2003; James and Lupton, 1978).

The problem can be even more complex if the stability of calcium sulfated mineral phases under different chemical or thermal conditions is considered. Calcium sulfate occurs in nature mainly in form of three different minerals distinguished by their degree of hydration: gypsum ($CaSO_4$), bassanite ($CaSO_4{\cdot}0.5H_2O$) and anhydrite ($CaSO_4$) (see Fig. 1). The changes from gypsum to anhydrite and back to gypsum are common processes (Klimchouk, 2000). This way, James (1992) noted that in very hot climates gypsum can dehydrate to anhydrite when it is exposed at the surface, above 42 °C, or where high salinity is present. The opposite process, dissolution of anhydrite and precipitation of gypsum, is also well documented. Thus, for example, Ramon and Alonso (2013),

* Corresponding author.
E-mail addresses: Juan.Alonso@uclm.es (J. Alonso), Marina.Moya@uclm.es (M. Moya), Vicente.Navarro@uclm.es (V. Navarro), Laura.Asensio@uclm.es (L. Asensio), jose.aguado@uclm.es (J.A. Aguado).

https://doi.org/10.1016/j.enggeo.2021.106049
Received 2 December 2019; Received in revised form 4 January 2021; Accepted 8 February 2021
Available online 14 February 2021

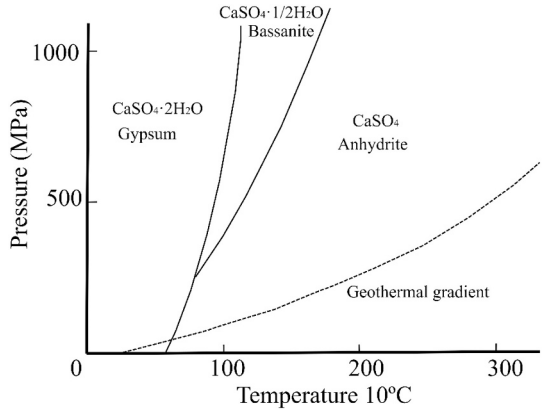

Fig. 1. Equilibrium diagram for the system $CaSO_4$-H_2O (Adapted from Zanbak and Arthur, 1986).

concluded that the modification of groundwater chemistry triggered the dissolution of anhydrite and the precipitation of gypsum under the piled foundations of a railway bridge, giving rise to heave.

Despite the extensive experimental study of the role of temperature in the dissolution of gypsum, the research on its impact to building foundations transmitting thermal loads is limited. In most cases, thermal loading of the ground is produced by heat loss from buildings and depends on the insulating quality of the envelope (Janssen et al., 2004; Weitzmann et al., 2005). Active thermal foundations can be considered as a particular case of ground heating from buildings (Kaltreider et al., 2015; Rempel and Rempel, 2013; Wang et al., 2016). In all these cases, heat losses are usually seasonal, as winter cycles are fully or partially compensated with the summer cycles, so that the overall heat balance of the system does not always produce a major change in temperatures beneath building foundations. In other cases, a permanent thermal load is imposed, and the seasonal damping is not possible, resulting in a continuous increase of the ground temperature over time. This is the case of some industrial facilities or power plants that host processes generating heat continuously over time.

The long-term prediction of the combined effect of thermal, chemical, mechanical and hydraulic changes on the foundation ground is not straightforward, since it involves processes that take place on a large space and time scale. The development of numerical models provides a very useful tool for its analysis if an adequate description of the constitutive behavior and a systematic acquisition of the parameters needed to quantify it are achieved. This allows to explore the interrelationships between physical and chemical processes, and to deepen in their relative importance in the system as a whole. Its interest could even be enhanced if used for fitting the parameters based on monitoring of ground movements, temperature, hydraulic and chemical changes during construction or commissioning of the work, as it would make possible to assess the system evolution and establish intervention frameworks on possible building damage, if necessary.

This is the approach followed in this paper, where the effect of a continuous thermal load through a building foundation on the response of a soil containing gypsum is analyzed. The study is based on the numerical model formulated in M4B (Alonso et al., 2016, 2019), a tool for

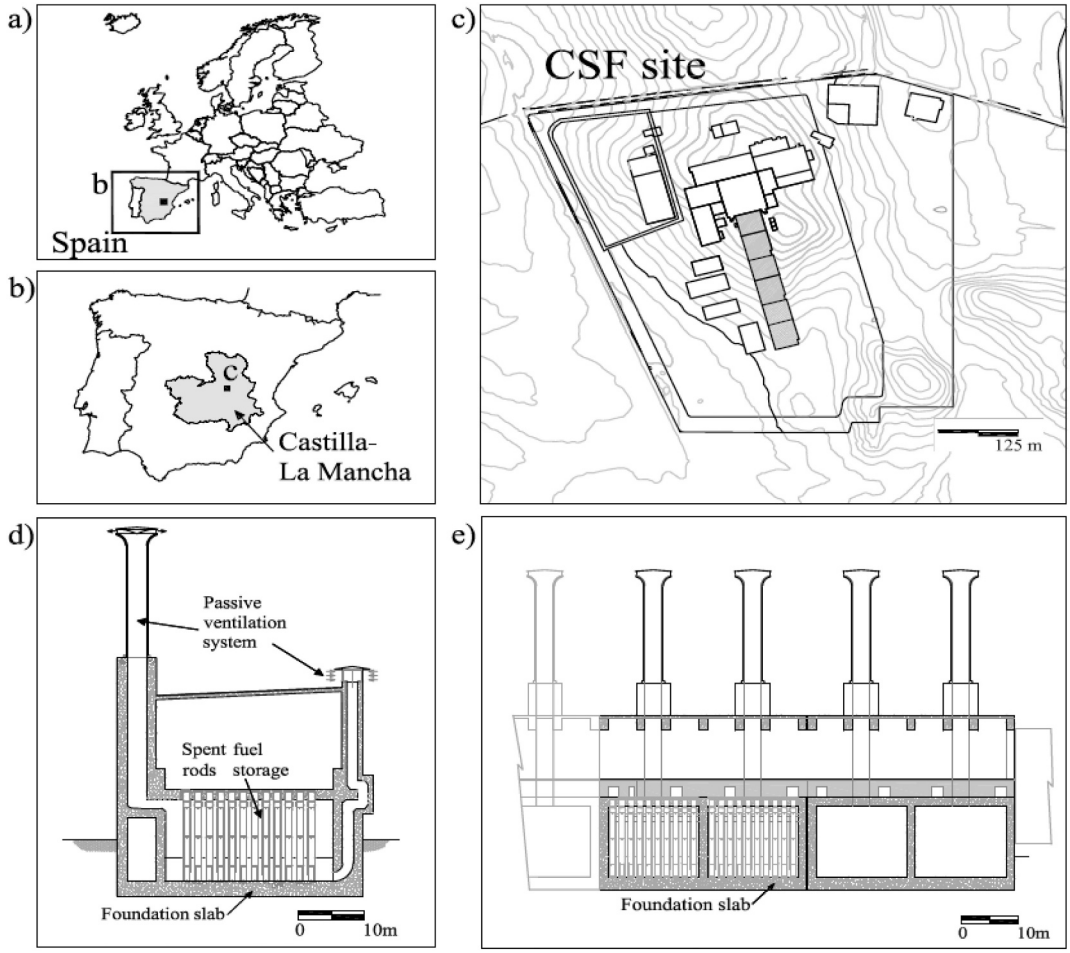

Fig. 2. Location of the CSF (a, b), and plan view of the facilities (c). The studied building is highlighted in grey. Cross (d) and longitudinal (e) sections of the building considered in the analysis.

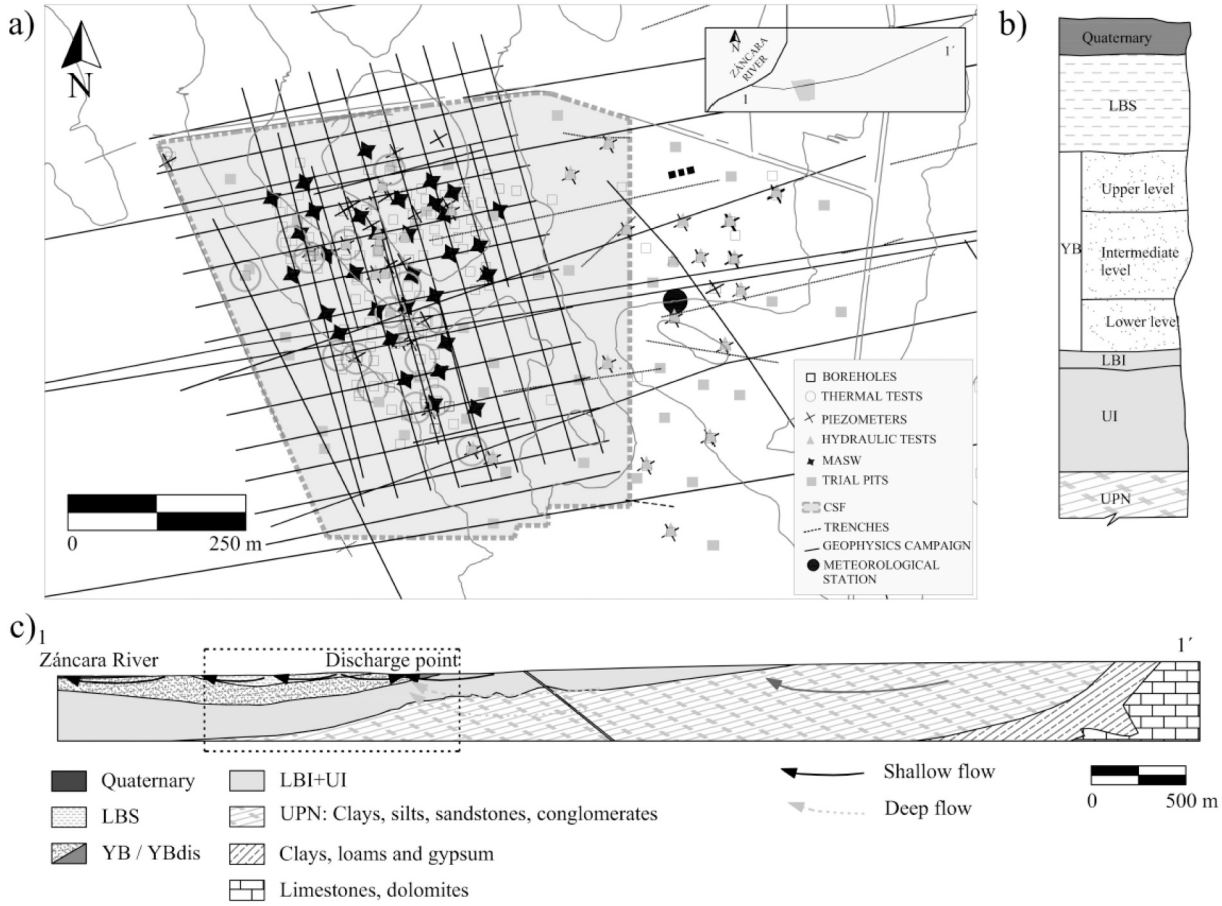

Fig. 3. (a) Location of the surveying works in the study area (CSF). (b) Stratigraphic profile for the study area. (c) Geological profile of the study area, showing idealized shallow and deeper water groundwater flow.

the definition of the differential equations that idealize the thermo-hydro-chemo-mechanical behavior of the ground and the foundation structure. Emphasis was placed on describing the temperature dependency of the dissolution processes of the calcium sulfated phases, as it constitutes the main research purpose of this work. The case of a building belonging to the facilities of the Spanish Central Storage Facility (CSF), planned near the village of Villar de Cañas, in central Spain, was considered (Fig. 2 a, b). This building (Fig. 2 c, d, e) will be the storage room for the high activity level radioactive waste of the Spanish nuclear power plants for a period of 60 years. The waste, mainly spent fuel rods, presents a high radiotoxicity and generates a considerable amount of heat, so special storage conditions are required. The main features of the site geological conditions are described in the next section. Afterwards, a conceptual and numerical model of the system is proposed. Finally, the importance of studying the effect of the dissipation of the thermal load through the ground on the building is highlighted, as well as the relative importance of various parameters on the response of the foundation.

2. Site description

2.1. Geology

For the geological characterization of the CSF site, a comprehensive field and laboratory survey was conducted by the Spanish public entity responsible of the management of radioactive waste, Enresa. These works, described in Cienfuegos et al. (2014) and Rueda et al. (2015), included geophysical prospecting campaigns (31,880 m of electrical tomography, 10,000 m of seismic reflection and a 10 × 20 m mesh of seismic tomography), the excavation of 3300 m in trenches for analysis of neotectonics of the study area, 53 trial pits and the drilling of near 189 geotechnical boreholes (9890 m). The boreholes were also used for the realization of 11 cross hole, 20 down-hole and 141 hydraulic tests. Also, 54 penetrometer tests, 33 multi-channel analysis tests of surface waves (or MASW) and 26 full wave sonic tests were performed (see Fig. 3a). The characterization study of the material and its behavior was attained in laboratory, with granulometry measurement, mineral identification and plastic index determination. Finally, oedometric, shear strength and swelling pressure behavior was also studied from undisturbed samples obtained in the boreholes.

Tertiary units and Quaternary deposits were recognized (Fig. 3b and c). The Neogene Tertiary materials include, from top to bottom, the Upper Balanzas Unit (LBS), the Balanzas Gypsum Unit (YB), the Lower Balanzas Unit (LBI) and the Lower Units (UI) (Fig. 3b). LBS are gypsum mudstones with a high compositional variability, with an average content of 32% in phyllosilicates and between a 30 to 60% in gypsum. YB Unit consists of a set of interbedded gypsum and mudstone layers with a wide mineralogical variability. Three levels can be distinguished within the YB Unit. The upper level is composed of gypsum, marls and mudstones, with a gypsum content close to 63%. The intermediate level presents macrocrystalline and laminated gypsum, about 84% of the mineralogical content on average, and a phyllosilicate content of 9%. The lower level corresponds to alabaster gypsum, present in decimetric levels alternating with marls and mudstone layers. The gypsum content at this level is around 42%. In the marls and mudstones of the LBI Unit, the predominant minerals are dolomite (33%), phyllosilicates (30%), and gypsum with an average content of 28%. The UI Unit is composed of mudstone-marls materials with the presence of lenticular gypsum

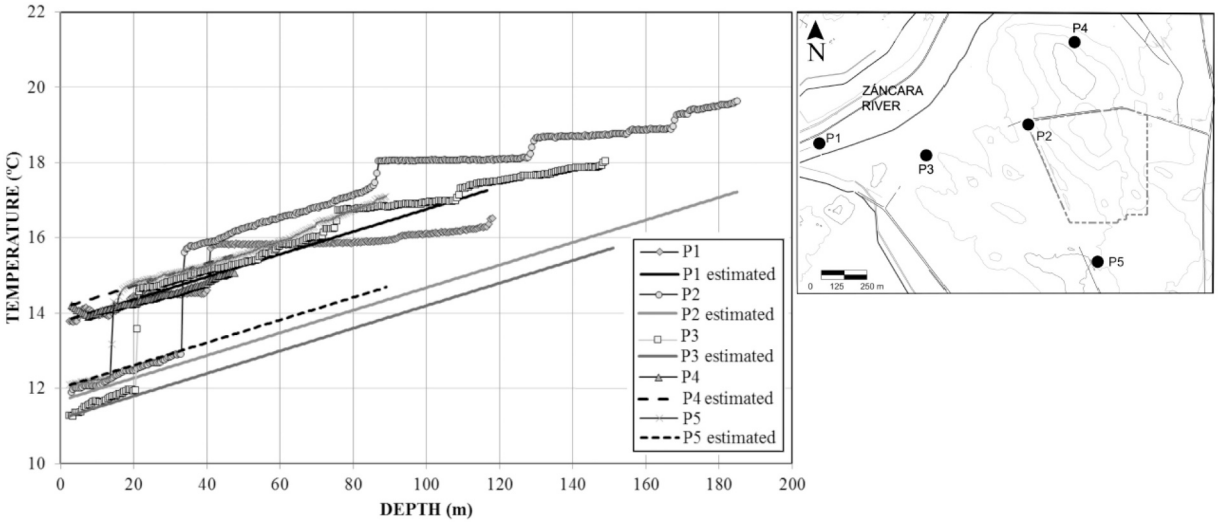

Fig. 4. Temperature measurements in boreholes (P1, P2, P3, P4, P5) and estimated general increase applying a thermal gradient of 0.03 °C/m.

crystals and sandstone levels. In the LBI and UI units, illite and muscovite are dominant among the clay minerals. Below all these units, clays, silts, sandstones and conglomerates of the Paleogene-Neogene Unit (UPN) were identified.

2.2. Hydrogeology

The main hydrogeological units were identified from the prospecting and testing campaign in the study area. Thus, 32 boreholes were established as piezometric control points, and 141 tests were carried out to estimate their hydraulic parameters. Of them, 105 were Lugeon tests, and the rest were pumping and pulse Slug tests, from which hydraulic conductivity and transmissivity values were estimated (Cienfuegos et al., 2014; Rueda et al., 2015). Also, for the characterization of the unsaturated behavior of the LBS unit, retention curves were obtained in laboratory with the vapor transfer technique (Pintado et al., 2009).

From the characterization campaign, it was concluded that a shallow and local water flow develops along low permeability Tertiary and Quaternary materials beneath the CSF facilities, besides a deeper and broader flow (Cienfuegos et al., 2014) from an aquifer system of high transmissivity in the Mesozoic carbonate materials (limestones and dolomites) located at the east of the CSF site (Fig. 3c). The main recharge is produced by infiltration of rain on the materials, and the main discharge is associated with the lateral drainage towards the alluvial of a river located to the west of the facilities (Záncara River, Fig. 3c), and occasionally and with less importance, in points of valley where more fractured or permeable materials emerge. In general, little significant flow exists under the planned facilities.

2.3. Hydrogeochemistry

The hydrogeochemical analysis is based on the sampling of 257 samples from Záncara River, 56 surface water monitoring points across the study area and 383 water samples and 106 geochemical profiles obtained in the boreholes.

All these data were managed by Gómez et al. (2014) to determine the main cations (Ca^{2+}, Mg^{2+} and Na^{+}), and anions (SO_4^{2-}, HCO_3^{-}, Cl^{-} and NO_3^{-}) in the pore waters, with some spatial variations in their concentrations. The correlation between the main cations (Ca^{2+}, Mg^{2+} and Na^{+}) and the sulfate anion (SO_4^{2-}) is practically 1:1 in the groundwater surrounding the study area, evidencing the major role of sulfates in their composition. Similarly, the ratio between SO_4^{2-} and Ca^{2+} concentration is 1:1 for almost all waters, up to a concentration of 30 meq/L (balance solution in equilibrium with gypsum), which indicates that gypsum is the predominant mineral phase in the system. Beyond this concentration, the SO_4^{2-} content in water continues to increase with no increase of Ca^{2+}, so that the further contribution of sulfate and precipitation of Ca^{2+} is controlled by other minority mineral phases (Alonso et al., 2019; Gómez et al., 2014).

2.4. Thermal characterization

Temperature measurements were recorded in boreholes carried out in the study area. For each borehole, the average temperature value was estimated for different depths, as shown in Fig. 4. A general increase of 0.03 °C/m in depth was observed from the records.

Furthermore, for the thermal characterization of the materials, a series of tests were carried out by Villar and Iglesias (2014) to estimate the thermal conductivities of samples from LBS and YB. The test results show a high variability even within the same unit, with a decrease in the conductivity values of the samples as the gypsum content increases.

3. Conceptual model

3.1. Formulation of the dissolution processes

Gypsum and anhydrite were considered in the model as minerals subjected to dissolution or precipitation under the effect of thermal loading. The former was found in every geological unit, as described in Section 2.1. Anhydrite, on the other hand, although not found in the ground proximity of the facilities, was considered in the model for dealing with possible mineral phase changes related to temperature variations. Among the calcium sulfated phases shown in Fig. 1, bassanite was not taken into consideration due to its low stability at the pressure and temperature conditions to be expected in the site.

The dissolution or precipitation of each mineral can be calculated from its saturation index, *SI*, being:

$$SI = log\frac{IAP}{K_{PT}} \tag{1}$$

where *IAP* is the ionic activity product of dissociated species and K_{PT} is the solubility product constant of the mineral. The solubility product of a mineral depends on pressure and temperature conditions. According to Appelo et al. (2014), an additive expression can be adopted:

$$logK_{PT} = logK_{P_0,T} - \frac{\Delta V_R}{2.303RT}(P - P_0) \tag{2}$$

Table 1
Polynomial terms for calculating solubility as a function of temperature.

Mineral	*A0*	*A1*	*A2*	*A3*	*A4*	*A5*
Anhydrite	5.009	-2.21×10^{-2}	−796.4	0	0	0
Gypsum	82.381	0	−3804.5	−29.9952	0	0

where $K_{P0,T}$ is the thermal component of the solubility product, ΔV_R is the volume change of the reaction (J/mol/kPa), T is temperature (K), P is pressure (kPa), P_0 is a reference pressure (kPa), and R is the gas constant (8.314 J/mol/K). The value of the pressure considered in Eq. 2 was considered to be equal to the stress P acting on the crystals (Zimmerman et al., 1994):

$$P = \frac{\sigma}{1-\phi} \tag{3}$$

where σ is the vertical total overburden stress and ϕ is the porosity.

Even if the gypsum-anhydrite chemical system has been widely studied, some uncertainties exist in the determination of precipitation conditions for anhydrite, fundamentally due to its slow crystallization kinetics (Ossorio et al., 2014). The theoretical transition temperature at which anhydrite becomes less soluble than gypsum is estimated by some authors to be between 42 and 60 °C (Freyer and Voigt, 2003), although some works determine this transition temperature for saline systems in a range below 52 °C (Hill, 1937; Posnjak, 1938). In this paper, the transition temperature at which anhydrite becomes less soluble than gypsum is given by the thermal component of the solubility product:

$$log K_{P_0,T} = A0 + A1\ T + \frac{A2}{T} + A3\ log\ T + \frac{A4}{T^2} + A5\ T^2 \tag{4}$$

where $A0$ to $A5$ are the fitting parameters shown in Table 1, adopted from Appelo (2015). The plot of the solubility product values against pressure and temperature according to Eqs. 2 to 4, for both gypsum and anhydrite, is shown in Fig. 5.

The conversion from gypsum to anhydrite occurs by the dissolution of the former and subsequent precipitation of the latter, not by alteration within the solid phase (Klimchouk, 2000). In this way, precipitation or dissolution rate for both minerals can be expressed by Lasaga's (1998) adapted expression:

$$R_{Min} = \kappa\ S_c\ \xi\ \phi_{Min} \left\{ \left| \frac{IAP}{K_{PT}} \right| - 1 \right\}^{\eta} \tag{5}$$

where R_{Min} is the precipitation/dissolution rate of each mineral, S_c is the specific surface, κ is the kinetic constant of dissolution/precipitation, ξ is the sign value indicating whether the process generates precipitation or dissolution of the mineral, ϕ_{Min} is the mineral volumetric fraction (V_{Min}/V_{TOT}, where V_{Min} is the mineral unit volume and V_{TOT} the total unit volume) and η is an empirical constant which depends on each dissolution or precipitation mineral reaction.

Finally, the calculation of the strain related to dissolution or precipitation of the sulfated phases, $d\varepsilon^{CH}$, can be considered through the following expression (Oldecop and Alonso, 2012):

$$d\varepsilon^{CH} = \sum_j \frac{W_j\ \gamma_j}{\rho_j} R_{Min,j} \tag{6}$$

where W_j is the molar mass, ρ_j is the density and γ_j expresses the fraction of volume displaced in the dissolution/precipitation process.

3.2. Numerical model

The equations proposed in the previous section, in addition to the balance equations summarized in Appendix A, defines a nonlinear system of coupled partial differential equations that, formulated as a boundary value problem, can be solved applying numerical techniques. The use of Multiphysics Partial Differential Equations Solvers, such as Comsol Multiphysics (Comsol, 2020) (CM) is a very useful option for the model described in this work. This software, based on the application of the finite element method with Lagrange multipliers, applies automatic symbolic differentiation techniques (Martins and Hwang, 2013) to obtain the derivatives needed to define the iteration matrix, significantly improving the computational convergence rate (Gobbert et al., 2009).

Although CM includes prebuilt models that allow to solve some problems without carrying out any numerical implementation, it also includes modules that do allow to define both the differential equations and the constitutive formulation. To freely introduce the model described in this paper, the second option was used in this work. Nevertheless, due to the high number of equations, variables, and parameters required for the complete definition of the model, this can become a difficult task. For this reason, the entire definition of the model was introduced in the M4B database (Alonso et al., 2016), developed to facilitate the implementation of the input files to be used in CM solver. By this approach, the researcher focuses on the definition of the physical problem and the software takes automatic control of assembling the system of equations and their solving.

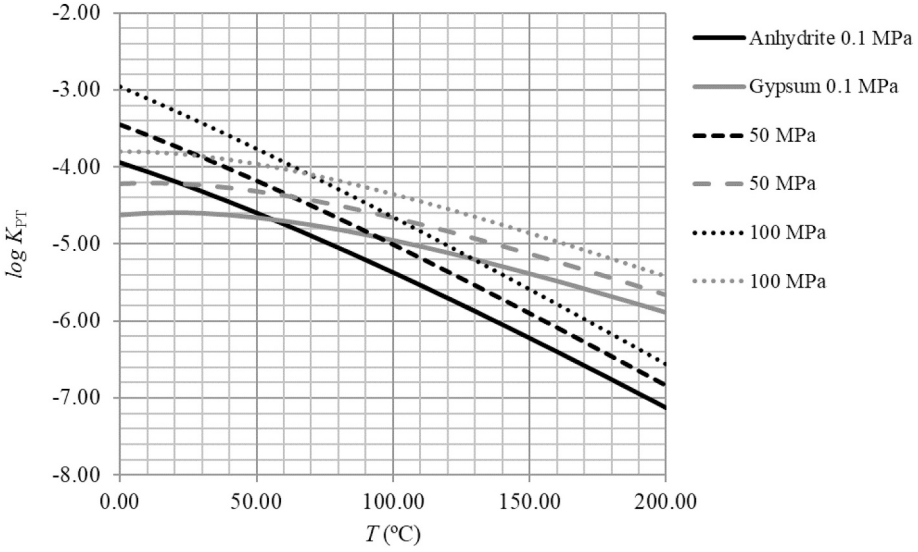

Fig. 5. Solubility product for gypsum (grey lines) and anhydrite (black lines).

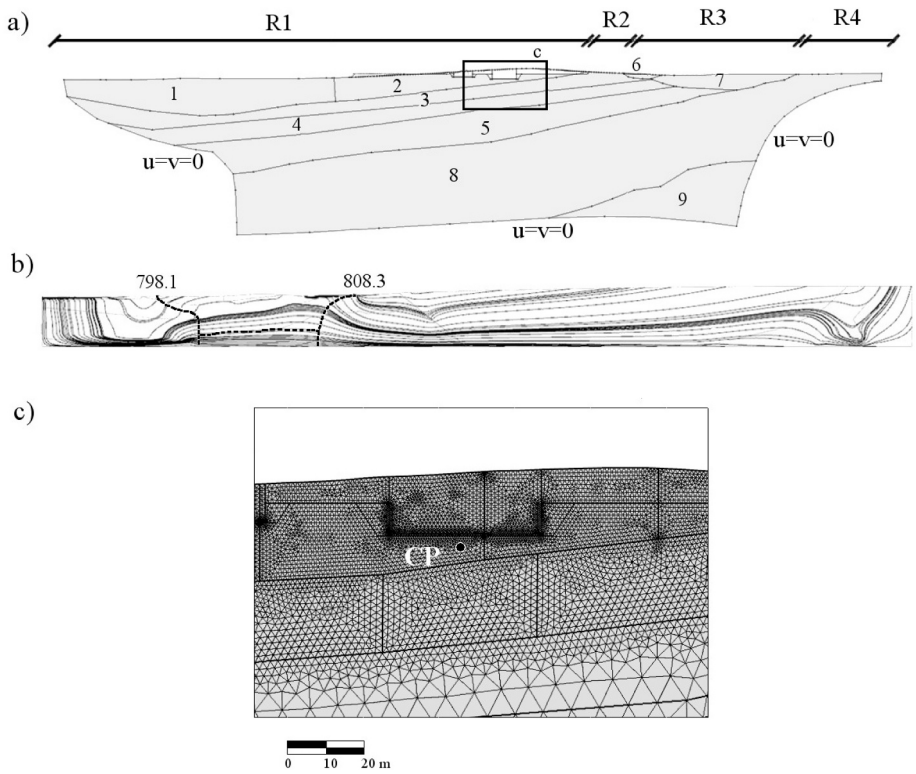

Fig. 6. a) Studied domain and boundary conditions. Inflow rates (R1 = 2 mm/yr, R2 = 2.5 mm/yr, R3 = 6.4 mm/yr, R4 = 3 mm/yr) and geotechnical units: 1 (LBS1), 2 (LBS2), 3 (NGYBa), 4 (NGYBb), 5 (YB1), 6 (Q), 7 (YBdis), 8(UI + LBI), 9 (UPN) are shown, b) potentiometric isolines and flow lines considered in the extended model for the definition of the study domain (dashed lines) and c) detail of the finite element mesh used in the analysis beneath the installations.

Further details of the numerical strategy and some engineering geology application examples used in CM for solving the equations implemented in M4B are given in Navarro et al. (2014a, 2014b, 2015, 2016) and Alonso et al. (2012a, 2012b, 2019).

3.3. Study domain, initial values and boundary conditions

The study domain in Fig. 6a was considered. Its geometry extends to where the effects of the thermal and hydraulic loads associated with the construction of the facilities can be considered negligible. For its definition it was necessary to solve the two-dimensional extended model of Fig. 6b, and to delimit the domain in which variations of temperature and liquid pressure were significant. By this approach, greater precision in the modeling of the surroundings of the facilities could be achieved (Fig. 6c). The isolines with the potentiometric head equal to 798.1 m at the western boundary, and 808.3 m at the eastern boundary, respectively, together with the bottom flow line identified in Fig. 6b, were established as the study domain limits. These isolines where considered in the model as Dirichlet boundary conditions, whereas the flow line in the bottom was considered as a zero-flow natural condition. Furthermore, according with Cienfuegos et al. (2014), an inflow rate value was imposed on the top boundary (R1 to R4, Fig. 4c). Finally, a Cauchy boundary condition was assigned to the discharge point shown in Fig. 3c. This condition is due to a natural drainage point in the out of plane direction.

The definition of boundary conditions and initial values for the thermal problem were based on the temperature measurements recorded in the boreholes. The gradient of 0.03 °C/m shown in Fig. 4 was considered. This can be considered as a common value in Earth science models (see, for example, Pollock, 1986). Surface temperature and its evolution outside the area affected by the construction of the facilities was obtained from the climate model studied by Enresa (2013), where data from 1966 to 2010 was analyzed. Based in this work, an increase in

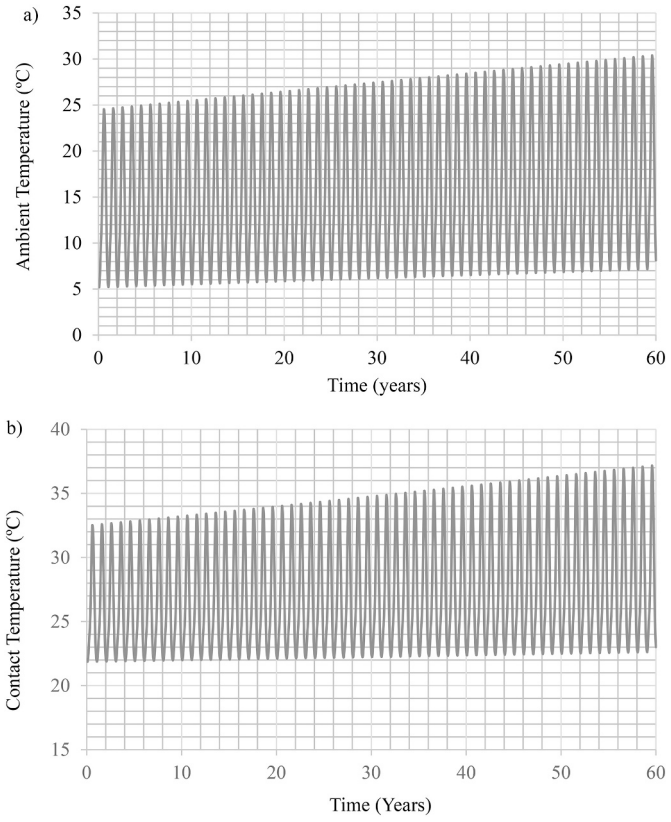

Fig. 7. Temperature prediction to 60 years under ambient conditions (a) and in the slab-ground contact (b).

Table 2
Parameters used in model. The data sources are summarized as follows: (1) Identified parameters, adapted from Cienfuegos et al. (2014, 2) Values fitted from average of tests in samples; (3) Geotechnical parameters from tests in Sondon (2016) and Rueda et al. (2015, 4) Estimated values consistent with the observed lithologies; (5) Value fitted from pedotransfer functions; (6) Parameters fitted from experimental data of Sondon (2016, 7) Parameters adapted of the model from Rueda et al. (2015, 8) fitted from experimental data of Villar and Iglesias (2014).

Par	K	ϕ_0	n_{VG}	a_{VG}	E	ν	k_s	λ_S
	Hydraulic conductivity	Initial porosity	n van Genuchten parameter	a van Genuchten parameter	Elastic modulus	Poisson's ratio	Stiffness to suction changes	Solid phase thermal conductivity
Units	m/s	–	–	(kPa^{-1})	kPa	–	1/kPa	W/mK
LBS1	5.20×10^{-8} (1)	0.30 (2)	1.40 (4)	1.4×10^{-4} (6)	6.5×10^{4} (6)	0.32 (3)	2.43×10^{-5} (7)	2.38 (8)
LBS2	2.00×10^{-9} (1)	0.30 (2)	1.40 (4)	1.4×10^{-4} (6)	6.5×10^{4} (6)	0.32 (3)	2.43×10^{-5} (7)	2.38 (8)
YB1 and NGYBa	2.54×10^{-9} (1)	0.16 (2)	1.89 (5)	1.4×10^{-4} (6)	4.2×10^{5} (7)	0.26 (3)	–	1.73 (8)
NGYBb	1.85×10^{-11} (1)	0.16 (2)	1.89 (5)	1.4×10^{-4} (6)	3.4×10^{6} (7)	0.27 (3)	–	1.73 (8)
Q	1.16×10^{-7} (1)	0.36 (3)	1.13 (5)	6.18×10^{-2} (4)	4.2×10^{5} (7)	0.30 (3)	–	2.60 (8)
YBdis	2.42×10^{-7} (1)	0.36 (3)	1.13 (5)	6.18×10^{-2} (4)	4.2×10^{5} (7)	0.30 (3)	–	2.60 (8)
LBI + UI	4.50×10^{-8} (1)	0.23 (2)	1.41 (5)	1.93×10^{-1} (4)	4.3×10^{4} (4)	0.30 (4)	–	2.49 (8)
UPN	3.70×10^{-8} (1)	0.23 (4)	1.41(4)	1.93×10^{-1} (4)	4.2×10^{5} (4)	0.30 (4)	–	2.49 (8)

the maximum monthly temperatures of 5 °C and an increase in the average minimum monthly temperatures of 2 °C were considered in view of the effect of climate change to 60 years, as shown in Fig. 7. This extrapolation was made from an initial temperature value of 14 °C, corresponding to the average annual temperature in Villar de Cañas (Enresa, 2013).

Three different cases were considered in this paper for defining the thermal boundary condition under the building. Two of these cases were based on the study performed by Enresa (2017), where the temperature value at the interface between the ground and the foundation slab was obtained from an Ansys-Fluent 3D analysis for different cases of ambient temperature and operation conditions. Thus, in a first case, H1, normal operation conditions of passive ventilation by natural convection of the building were considered, and the relationship given in Eq. 7 was adopted.

$$T_{\text{Interface}}(^{o}\text{C}) \begin{cases} \text{If } T_{\text{Ambient}} \geq 14^{o}\text{C}, T_{\text{Interface}} = 0.851\ T_{\text{Ambient}} + 13.0\,^{o}\text{C} \\ \text{otherwise}, T_{\text{Interface}} = 0.2\ T_{\text{Ambient}} + 23.2\ \ ^{o}\text{C} \end{cases} \quad (7)$$

By combining this equation with the ambient temperature prediction to 60 years from Fig. 7a, the temperature prediction shown in Fig. 7b was obtained. Consequently, the maximum reached temperature was 36 °C. In the second case, H2, a temperature of 60 °C was set in the ground-slab interface, corresponding to the maximum temperature reached in case of accidental malfunction of the natural ventilation of the building Enresa (2017). It is important to note that, as the building design considers passive ventilation through natural convection, the temperature reached in the H2 Case would only correspond to an accidental situation. Therefore, the consideration of permanent conditions for the thermal loads in the H2 Case is an unrealistic scenario given the actual design of the building. This work considers this case only as a reference frame for the hypothetical case of a non-ventilated building, where temperature at which anhydrite is less soluble than gypsum would be reached. Furthermore, in both cases (H1 and H2), a very conservative criterion was adopted, as the cooling of the fuel rods was disregarded, and the maximum temperature value obtained by Enresa (2017) at any point of the slab was considered. Finally, a third case disregarding thermal loads under the building, H0, was also performed to be used as a reference for comparison purposes.

A non-diffusion mass flow condition was considered for the hydrogeochemical problem at the western boundary. In the eastern and upper boundaries, Dirichlet type conditions were imposed. The concentration values of the species corresponding to a fresh water (ie. with a low content of dissolved soluble salts) were considered. Finally, a zero-flow natural condition was considered in the lower boundary. The chemical species considered in the numerical model (H^+, CO_3^{2-}, SO_4^{2-}, Ca^{2+}, Mg^{2+}, Na^+, K^+, Cl^-, HCO_3^-, OH^-, H_2CO_3, $CaCO_3$, $CaHCO_3^+$, $MgHCO_3^+$, $MgCO_3$, $NaHCO_3$, $NaCO_3^-$, HSO_4^-, H_2SO_4, $CaHSO_4^+$, $CaSO_4$, $MgSO_4$, $NaSO_4^-$, $CaOH^+$, $MgOH^+$, NaOH, KOH) were based on the hydrogeochemical analysis performed by Gómez et al. (2014) and Alonso et al. (2019).

For the mechanical problem, null displacement conditions were assumed on the bottom and lateral boundaries, and free displacement condition was considered on the upper boundary of the model. A 2.5 m thick slab, with a total load of 375 kPa was considered under the building. This value includes the dead-weight of the building and the operation loads.

3.4. Model stages

Two stages were computed to get stable initial conditions prior to the setting up of the facilities. In a first stage, the groundwater flow regime and chemical speciation in natural conditions (prior to the excavation) were obtained, allowing to reproduce the chemical data obtained in field and laboratory tests. A detailed description of the obtention of the hydrogeochemical initial conditions is provided in Alonso et al. (2019). In a second stage, the excavation process of 100 days up to the proposed depth was simulated. This was performed by a smooth function that progressively cancels the effects of the volumetric forces (weight), elastic modulus (stiffness) and hydraulic conductivity of the excavated materials (blank area in Fig. 6a). This process modifies the mechanical response and the flow rate regime, so it had to be taken into account for the definition of the initial condition of the final stage, where the setting up of the facilities was simulated. This was done by imposing the mechanical and thermal loads exerted by the building over a period of 60 years. Similar to the excavation stage, this was done through functions describing the activation of the flexural rigidity and the density of the slab, plus the service loads transmitted by the building, over a period of 3 months estimated for its construction. Finally, to consider the hydraulic barrier effect of the paved area, a recharge value of zero was applied in the area surrounding the facilities.

3.5. Thermal, hydraulic and mechanical parameters

The permeability values assigned for the different units were

adjusted to fit the piezometric level measurements described in Section 2.2. Parameters for the retention curve, according to the van Genuchten (1980) model, and relative permeability were obtained from laboratory tests described in Section 2.2. Hydraulic parameters used in the model are given in Table 2.

Thermal conductivities of the units considered in the model were obtained from the laboratory tests enumerated in Section 2.4 of this paper. These show a high variability in thermal conductivity values, mainly related to the influence of gypsum content. The interpretation of the results allowed to fit the value of the thermal conductivity of the solid phase for the different units shown in Table 2. For this purpose, Eq. A16 in Appendix A was used, considering the averaged contribution of different components (soil, air and water), according to Gens (2010). In this equation, a value of 0.6 W/(mK) was considered for the thermal conductivity of water, λ_W, and a value of 0.024 W/(mK) was adopted for the air, λ_A (Gens, 2010). The latent heat of vaporization (see Appendix A) considered in the model was 2500 kJ/kg (Pollock, 1986). Furthermore, a specific heat of 1.01 kJ/(kg K) for air, 1.89 kJ/(kg K) for vapor, 4.18 kJ/(kg K) for water, and 0.837 kJ/(kg K) for solid from Pollock (1986) were considered in the analysis.

The elastic modulus, Poisson's ratio and stiffness to suction changes values shown in Table 2 were fitted from the experimental data in Sondon (2016) and Rueda et al. (2015).

3.6. Dissolution/precipitation kinetics and bulking coefficient

For the dissolution/precipitation problem, the value of R_{Min} in Eq. 5 is controlled by the $\kappa \cdot S_c$ product. The rate constant, κ, on one hand, has been investigated by several authors, providing a relatively wide range of values, in the order of 10^{-4} mol/m^{2}s for gypsum dissolution (Barton and Wilde, 1971; Colombani, 2008) and one to two orders of magnitude smaller for the dissolution of anhydrite and precipitation of gypsum (James and Lupton, 1978; Kontrec et al., 2002). Despite the significant amount of research effort dedicated to the bulk growth of gypsum from aqueous solutions, much less has been that devoted to understanding the growth mechanisms and kinetics of anhydrite, and no bulk growth rate data are available for this phase (Van Driessche et al., 2019). Nevertheless, experimental observations show that the growth dynamics of the main faces of anhydrite is approximately two orders of magnitude slower than gypsum (Ossorio et al., 2014; Van Driessche et al., 2019). Despite the broad experimental research regarding rate constants for gypsum dissolution/precipitation and anhydrite dissolution, it should be noted that experimental results obtained in idealized laboratory conditions may differ from realistic field values (Ramon and Alonso, 2013). On the other hand, the specific surface S_c of the $\kappa \cdot S_c$ product depends in turn on the amount of mineral species present in the rock at the time, the shape and the size of the crystals or nodules (Oldecop and Alonso, 2012), so its determination is not straightforward either. For achieving more realistic values, Ramon and Alonso (2013) obtained the $\kappa \cdot S_c$ product value from back-analysis of field heave record of mudstones bearing calcium sulfate minerals, and linked the dissolution/precipitation rate with this value and the volume fractions of the mineral, as shown in Eq. 5. In the absence of more reliable experimental results, the product value obtained by these authors ($\kappa \cdot S_c = 2.03 \times 10^{-3}$ mol/m^{3}s) was adopted in this work as the reference value for both gypsum and anhydrite rate reactions. Since the limiting process seems to be the precipitation of anhydrite, this value can be considered as a conservative reference, as this reaction was not considered in the work of Ramon and Alonso (2013). However, given the uncertainty associated with these parameters, this value is considered appropriate for the purpose of this paper. The description for the initial mineral fraction values in Eq. 5, ϕ_{Min}, on the other hand, is given in Alonso et al. (2019). For the case of gypsum in the LBS unit, an initial value of $\phi_{Min,Gypsum} = 0.4$ was considered. For anhydrite, an initial content of zero was specified, although a minimum reaction rate product value of $\kappa \cdot S_c \cdot \phi_{Min,Anh} = 3.47 \times 10^{-7}$ mol/m^{3}s was defined in case of anhydrite supersaturation. This value approximately reproduces the rate of anhydrite nucleation obtained in the work of Wagner et al. (2005).

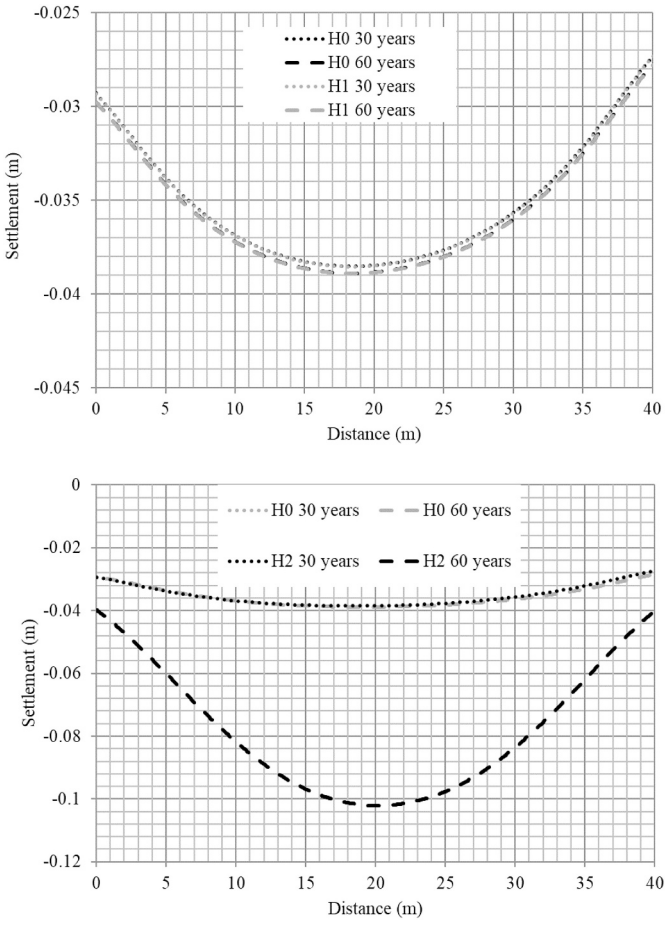

Fig. 8. Settlement under the slab for cases H1 (a) and H2 (b), 30 and 60 years after construction of the building.

The empirical constant η in Eq. 5 depends on each dissolution or precipitation mineral reaction. In the case of gypsum, its dissolution rate follows a first-order equation ($\eta = 1$) (Liu and Nancollas, 1971; Zdanovsky, 1956), whereas the dissolution rate of anhydrite obeys a second-order equation ($\eta = 2$) (James and Lupton, 1978; Kontrec et al., 2002). On the other hand, the growth of gypsum crystals was observed to follow a second order ($\eta = 2$) expression (Kontrec et al., 2002; Witkamp et al., 1990). Although the precipitation rate of anhydrite seems to be less studied, a first-order expression for anhydrite precipitation was obtained by Meijer (1983) in laboratory conditions ($\eta = 1$). Therefore, first-order equations were considered in this work both for gypsum dissolution and anhydrite precipitation.

γ, defined in Eq. 6, is a coefficient measuring the bulking effect induced by crystal growth in the rock mass. This parameter has been obtained by some authors from fitting of field measurements (Oldecop and Alonso, 2012; Ramon and Alonso, 2013). Ramon et al. (2017) also evaluated this parameter from laboratory data reported by Huber et al. (2015). In all these cases, forensic analysis was carried out considering the anhydrite dissolution and gypsum precipitation problems. In this work, a reasonable range of gamma values was considered according to conclusions reached by these authors. A value of $\gamma = 1$ was adopted in the reference model, which implies that shrinkage/swelling is equal to the dissolved/precipitated mass. Additionally, a sensitivity analysis was also completed, so further models with $\gamma = 0$ (all the dissolution/precipitation is produced in the existing voids), and $\gamma = 0.5$ (intermediate situation) were also analyzed.

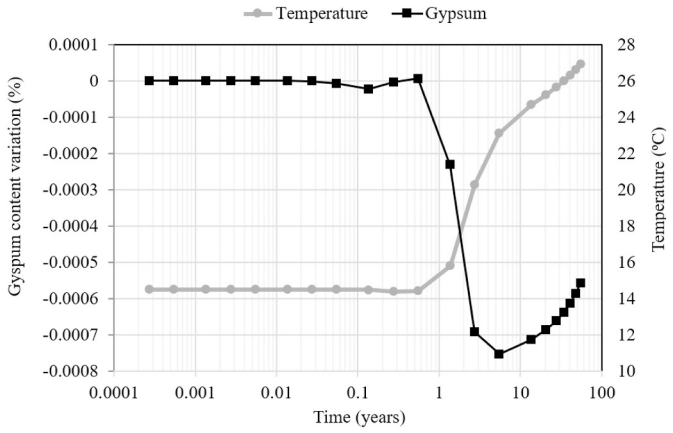

Fig. 9. Gypsum content and Temperature variation in point CP shown in Fig. 6 (Case H1).

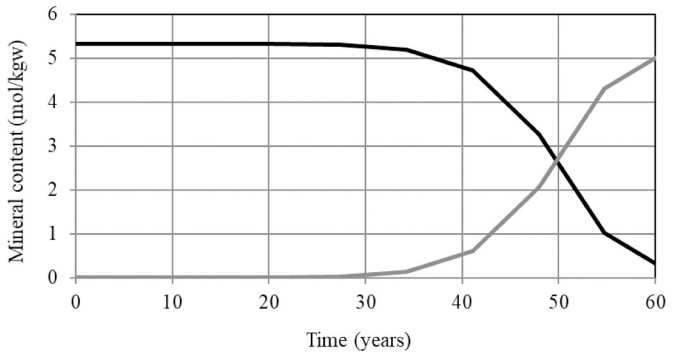

Fig. 10. Gypsum (black) and anhydrite (grey) content evolution for Case H2 in point CP shown in Fig. 6.

4. Results and discussion

4.1. Settlement of the slab

Settlement of the slab for cases H1 and H2, after 30 and 60 years from the construction of the facilities, are shown in. Fig. 8. The settlement profile without thermal load is also shown as a reference (H0). Vertical displacements in Case H2 are much higher than those experienced in Case H1, since the former occur without gypsum-anhydrite transformation. Furthermore, H1 and H0 profiles show a settlement increase towards the western part of the slab (Fig. 8a). This is a consequence of the higher compressibility and thickness of the LBS Unit beneath the building in that area, as opposed to YB unit, as it provides a larger amount of settlement. On the other hand, differences in settlement evolution between cases H1 and H0 are linked to gypsum dissolution. As shown in Fig. 9, after 200 days, the temperature growth predicted in point CP under the building (shown in Fig. 6) is followed by an increase of the gypsum solubility according to temperature-solubility relation in Eq. 4, leading to its dissolution. Five years after the setting up of the facilities, the temperature at which gypsum exceeds its maximum solubility product is reached, and thereafter precipitation occurs. At the end of the process (60 years), the dissolution of gypsum in the early years is higher than the overall precipitation, and settlement remains beneath the slab. Nevertheless, differences between Case H1 and H0 are very low, and can be considered as negligible for design or construction purposes.

Settlements calculated in Case H2 are higher than those calculated for Case H1. The differences are a consequence of the large volume reduction experienced in the ground in Case H2: as gypsum occupies a larger unit volume than anhydrite, the volume change is linked to the differences of density between the mineral phases, the total amount of gypsum and anhydrite to be dissolved or precipitated, and parameter γ in Eq. 6. With temperature increase, the anhydrite solubility product decreases faster than the gypsum solubility product, becoming lower than the latter above 45 °C in the adopted model. As a result, anhydrite precipitates from calcium sulfate, undersaturating the solution with respect to gypsum and leading to its dissolution. This process is self-feeding, and anhydrite precipitation and gypsum dissolution take place simultaneously, as shown in Fig. 10. The gypsum-anhydrite transformation is linked to the heat transfer under the foundation, but also to the evolution of their dissolution/precipitation kinetics. In point CP, for Case H2, this transformation begins after 30 years from construction of the facilities. Nevertheless, model results show that angular distortion in all cases would be under the 1/150 limit and would not cause structural damage according to EN 1997–1 (2004).

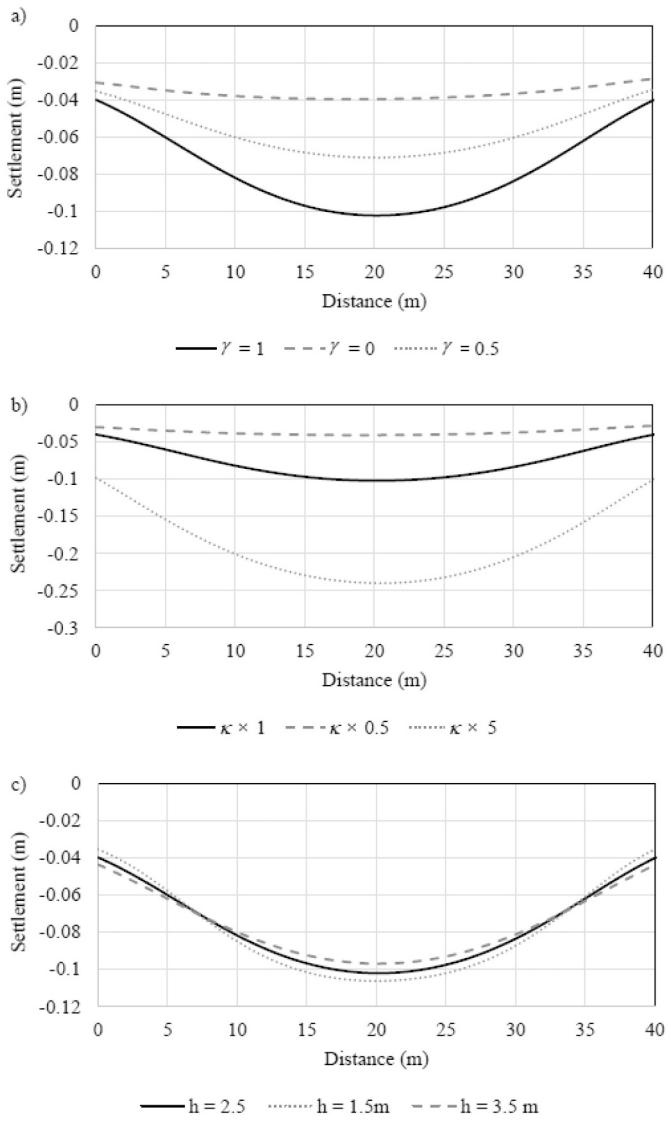

Fig. 11. Settlement for different values of (a) gamma parameter, (b) precipitation/dissolution rate and (c) slab thickness.

4.2. Sensitivity analysis inspection

The relevance of the processes described in this paper depends on a large extent on the value of the parameters used in the model. An inspection of the sensitivity of the model response against parameter γ

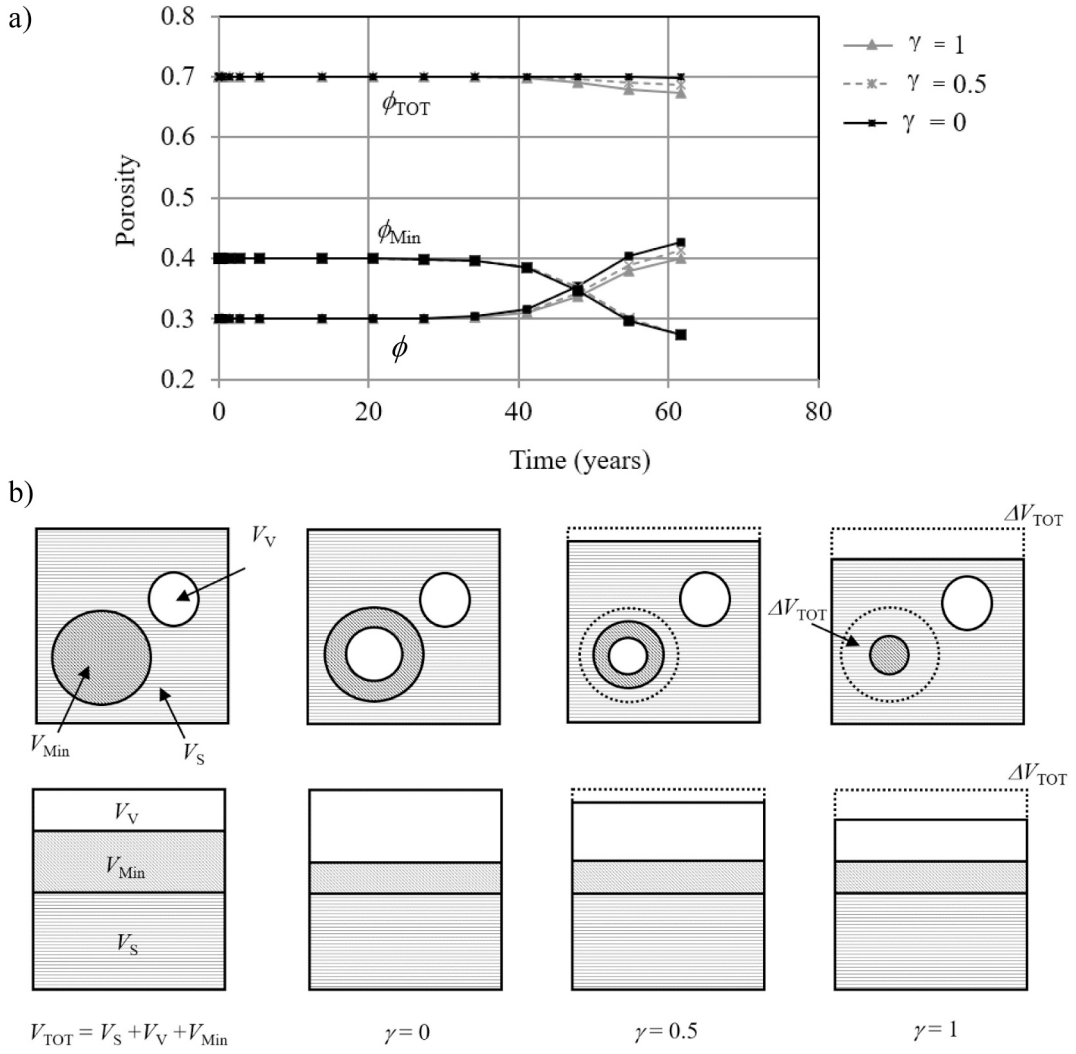

Fig. 12. a) Porosity evolution in CP. b) Schematic description of the dissolution process as a function of γ.

described in Eq. 6, the precipitation/dissolution rate (Eq. 5) and the flexural rigidity of the slab foundation was performed for Case H2.

The influence of parameter γ is shown in Fig. 11a. For low γ values, smaller vertical displacements would be produced. This is because low γ values imply that almost all minerals dissolve or precipitate in the free porosity of the soil, with very limited impact on the deformation of the medium. On the other hand, high values of γ mean that a fraction of the volume needed to host the crystals during the process of dissolution or precipitation would be obtained by the partial displacement of the solid skeleton, and not only through variations of free porosity, developing higher stress changes which would lead to higher displacements as well.

Fig. 11b shows the values of the vertical displacements for different precipitation/dissolution rates of both gypsum and anhydrite. For lower rates of the $\kappa \cdot S_c$ product ($\kappa \times 0.5$), smaller vertical displacements would develop under the slab, whereas for higher rates ($\kappa \times 5$), much larger vertical displacements are produced. The relative effect of the $\kappa \cdot S_c$ product is explained by the amount of soil where the process of dissolution of gypsum and precipitation of anhydrite is fully developed. This way, the higher the value of $\kappa \cdot S_c$, according to the conceptual model described in Section 3.1, the larger volume of soil under the building would be affected by the gypsum-anhydrite transformation. For low values, on the other hand, the slow kinetics of the process reduces the soil volume under the building where the gypsum-anhydrite transformation has had enough time to take place. From this sensitivity analysis, it is shown that the effect of the $\kappa \cdot S_c$ product on the foundation response is major in comparison with the other evaluated parameters. However, it should be noted that, as described in Section 3.6, a conservative reference parameter has been considered in the analysis, so higher values than the reference $\kappa \cdot S_c$ product adopted in this paper are unlikely to occur. Nevertheless, further research is needed for a reliable estimation of these parameters to conduct more accurate predictions of these processes.

Finally, Fig. 11c shows the distribution of vertical displacements in the slab under the building considering slab thicknesses of 1.5, 2.5 and 3.5 m. An increase of the slab stiffness would lead to the development of more reduced vertical displacements in the center of the slab. It should also be noted that a thicker slab would also improve the thermal dissipation of temperatures transmitted from the building.

4.3. Dissolution/precipitation process and porosity evolution

As has been seen in the previous section, γ would largely condition the volumetric behavior of the soil under the building in case H2. The evolution of free porosity ($\phi = V_V/V_{TOT}$), mineral volumetric fraction ($\phi_{Min} = V_{Min}/V_{TOT}$), and total porosity ($\phi_{TOT} = \phi + \phi_{Min}$) at control point CP, for the different values of γ considered in the sensitivity analysis, is shown in Fig. 12a. Although the changes in total porosity in Fig. 12a are also related to the stress-strain path derived from the building construction, its influence is minor compared to the effect of the dissolution and precipitation process. This is shown the same figure, as variations in

porosity are very small up to 40 years from the ending of the construction works, when the process of dissolution of gypsum and precipitation of anhydrite develops. To facilitate interpretation, this process, for the different values of γ, is schematized in Fig. 12b. For the case of $\gamma = 0$, there would not be a variation of the reference volume V_{TOT}, since no bulking effect would occur because of the dissolution/precipitation process. Thus, there would be an increase in the free porosity, ϕ, at the expense of a reduction in ϕ_{Min}, so that the total porosity, ϕ_{TOT}, would remain constant. In the case of $\gamma = 0.5$, the loss of mineral volume would lead to a half of that loss in the reference volume (V_{TOT}). In this case, there would be a reduction of total porosity (see Fig. 12a). Finally, for the case of $\gamma = 1$, all the net volume lost because of gypsum dissolution and anhydrite precipitation would originate the loss of the same amount of the total volume. Although the volume of voids would remain invariable, there would be a net increase in ϕ because of the reduction of the reference volume, V_{TOT}.

5. Conclusions

In this paper, the effect of a thermal load on a soil containing gypsum, in the facilities of the Spanish Central Storage Facility (CSF), is analyzed. Based on the considerations described above, it is concluded that:

a) With the passive ventilation design of the building, a moderate thermal load would be produced (Case H1), and its effect on dissolution leads to a minor modification of the settlement of the foundation slab.
b) In the hypothetical case of absence of ventilation in the building design, higher thermal loads would develop (Case H2), and a change of mineral phase in calcium sulfate might occur. This would favor the dissolution of gypsum and precipitation of anhydrite, leading to a loss of unit volume that could cause larger settlement of the slab.
c) Model results show that angular distortion in all cases would be under the 1/150 limit and would not cause structural damage according to EN 1997–1 (2004).
d) Sensitivity analysis shows a significant dependence of the vertical displacements on parameter γ, as well as on the dissolution/precipitation rate of the mineral phases, whereas the dependence on the slab thickness is minor.
e) Design measures adopted in building design and considered in this work, such as flow and thermal barriers, or an effective passive ventilation system, minimize possible adverse effects resulting from a potential gypsum - anhydrite transformation.

Declaration of Competing Interest

None.

Acknowledgements

This research work has been carried out under the framework of the collaborative agreement between the University of Castilla La-Mancha and the public company Enresa (Empresa Nacional de Residuos, S.A.).

Appendix A. Equations

The equations for water flow problem are summarized in Table A1.

Table A1
Hydraulic equations.

Description	Equation	#
Water mass balance equation	$\frac{\partial m_W}{\partial t} + \nabla\cdot(m_W \mathbf{v}_W) = 0$	[A1]
Total mass of water	$m_W = m_L + m_V = \rho_W Sr\ \phi + \rho_V(1 - Sr)\ \phi$	[A2]
Water mass flow	$m_W \mathbf{v}_W = m_L \mathbf{v}_L + m_V \mathbf{v}_V$	[A3]
Mass liquid flow	$m_L\ \mathbf{v}_L = m_L\ \mathbf{v}_S + \rho_W \mathbf{q}_L$	[A4]
Advective component of fluid flow	$\mathbf{q}_L = -\frac{\mathbf{K}_L\ k_{rL}}{\mu_L}(\nabla P_L + \rho_W\ g\ \nabla z)$	[A5]
Vapor mass flow	$m_V\ \mathbf{v}_V = m_V\ \mathbf{v}_S + \mathbf{j}_V$	[A6]
Mass diffusion of vapor	$\mathbf{j}_V = \phi\ (1 - Sr)\ \tau\ D\ \nabla \rho_V$	[A7]

In Eq. A2, $\phi$is the porosity, ρ_W and ρ_V are the density of liquid water and vapor, respectively, and Sr is the degree of saturation of the liquid phase, obtained with the van Genuchten (1980) model. For the definition of the mass liquid flow, P_L is the liquid pressure, v_S is the deformation velocity of the solid skeleton, z is the vertical coordinate and K_L, k_{rL} and μ_L are the intrinsic permeability, relative permeability and dynamic viscosity of the liquid, respectively. D is the molecular diffusion coefficient and τ is the tortuosity, considered for the calculation of the mass diffusion of vapor according to Fick's Law.

Thermal equations are summarized in Table A2. In Eqs. A10 to Eq. A13, c_L, c_V, c_A, and c_S are the specific heat of liquid, vapor, air and solid, respectively, T_o is a reference temperature, and h_V^0 is the latent heat of vaporization/condensation.

A detailed explanation of the implementation and solution of the chemical equations solved in the model is given in Alonso et al. (2019). The governing equations are summarized in Table A3. In Eq. A18, m_i is the number of moles of species "i" per unit volume of solution and $m_{Min,j}$ is the amount of species precipitated as mineral "j". N and M are the number of species and minerals, respectively. R_i is the net production rate of the chemical species due to chemical reactions and $R_{Min,j}$ is the net production rate due to dissolution/precipitation. β_{ji} defines if species "i" is effectively related to mineral "j" ($\beta_{ji} = 1$) dissolution/precipitation processes or not ($\beta_{ji} = 0$). In Eq. A20, D_i is the diffusion coefficient of species "i".

Equations for the mechanical problem are shown in Table A4. σ_{TOT} is the total stress vector, ρ is the bulk density and m is the vector expression of the Kronecker delta. In the definition of the reference pressure (see Gens, 2010, for example), P_L and P_G are the liquid and gas pressure, respectively. $d\varepsilon$ is the incremental strain and D^e is the elastic matrix. In the definition of the elastic strain variation due to suction variations, P_{atm} is the value of atmospheric pressure and κ_S is the stiffness of the soil against suction changes, S. Strain due to the precipitation or dissolution of minerals, $d\varepsilon^{Ch}$, is calculated with Eq. 6.

Finally, the behavior of the building foundation was considered with the beam formulation available in the "Structural Mechanics Module" of CM (Comsol, 2020).

Table A2
Thermal equations.

Description	Equation	#
Energy conservation equation	$\frac{\partial h}{\partial t} + \nabla \cdot \mathbf{l}_H = 0$	[A8]
Internal energy of the porous medium	$h = \rho_W Sr\phi h_L + \rho_V \phi(1-Sr)h_V + \ldots + \rho_A \phi(1-Sr)h_A + \rho_S(1-\phi)h_S$	[A9]
Internal energy of liquid	$h_L = c_L(T - T_O)$	[A10]
Internal energy of vapor	$h_V = h_V^0 + c_V(T - T_O)$	[A11]
Internal energy of air	$h_A = c_A(T - T_O)$	[A12]
Internal energy of solid	$h_S = c_S(T - T_O)$	[A13]
Heat flow	$\mathbf{l}_H = \mathbf{l}_{HC} + \mathbf{l}_{HA}$	[A14]
Conductive heat flow	$\mathbf{l}_{HC} = -\lambda \nabla T$	[A15]
Thermal conductivity	$\lambda = \lambda_S^{(1-\phi)}\lambda_L^{Sr\phi}\lambda_A^{(1-Sr)\phi}$	[A16]
Advective heat flow	$\mathbf{l}_{HA} = h_L\rho_W(\mathbf{q}_L + Sr\phi\mathbf{v}_S) + \ldots + h_V\rho_V(\mathbf{j}_V + Sr(1-\phi)\mathbf{v}_S) + h_S\rho_S(1-\phi)\mathbf{v}_S$	[A17]

Table A3
Chemical equations.

Description	Equation	#
Chemical species mass balance equations	$\frac{\partial(\phi\ Sr\ m_i)}{\partial t} + \nabla\cdot(\phi\ Sr\ m_i\ \mathbf{v}_i) = \ldots$ $\ldots = \phi\ Sr\ R_i - \sum_{j=1}^{M}\phi\ Sr\ \beta_{ji}\ R_{Min,j}$ $\frac{\partial(\phi\ Sr\ m_{Min,j})}{\partial t} = \phi\ Sr\ R_{Min,j}$ $i = 1,\ldots,N$ $j = 1,..,M$	[A18]
Molar flow per unit area	$\phi\ Sr\ m_i\ \mathbf{v}_i = \phi\ Sr\ m_i\ \mathbf{v}_S + m_i\ \mathbf{q}_L + \mathbf{j}_i$	[A19]
Molecular diffusion	$\mathbf{j}_i = -\phi\ Sr\ D_i\ \nabla m_i$	[A20]

Table A4
Mechanical equations.

Description	Equation	#
Equilibrium equation	$\nabla\cdot\boldsymbol{\sigma}_{TOT} - \rho g \nabla z = 0$	[A21]
Constitutive stresses	$\boldsymbol{\sigma} = \boldsymbol{\sigma}_{TOT} - P_\phi\ \mathbf{m}$	[A22]
Reference pressure	$P_\phi = \max(P_G, P_L)$	[A23]
Constitutive behavior	$d\boldsymbol{\sigma} = \mathbf{D}^e(d\varepsilon - d\varepsilon^S - d\varepsilon^{Ch})$	[A24]
Elastic strain due to suction variations	$d\varepsilon^S = \frac{1}{3}\frac{\kappa_S}{(S + P_{atm})}dS\mathbf{m}$	[A25]
Void ratio	$\frac{\partial e}{\partial t} + \mathbf{v}_S\cdot\nabla e = (1+e)\nabla\cdot\mathbf{v}_S$	[A26]

References

EN 1997–1, 2004. (English): Eurocode 7: Geotechnical design - Part 1: General rules. The European Union Per Regulation 305/2011, Directive 98/34/EC, Directive 2004/18/EC.

Enresa, 2013. Estudio meteorológico del emplazamiento del Almacén Temporal Centralizado (ATC) de Villar de Cañas Technical Report: 042-CO-SU-2012-0002_IF-01_Rev4.docx. AItemin-Enresa.

Enresa, 2017. Cálculo de la distribución de temperaturas en los muros del Edificio de Almacenamiento de Combustible Gastado y RAA. Technical Report: N°: 042-L1-FC-M-50500.

Kontrec, J., Kralj, D., Brečevic, L., 2002. Transformation of anhydrous calcium sulphate into calcium sulphate dihydrate in aqueous solutions. J. Cryst. Growth 240, 203–211. https://doi.org/10.1016/S0022-0248(02)00858-8.

Alonso, J., Navarro, V., Calvo, B., 2012a. Flow path development in different CO_2 storage reservoir scenarios: a critical state approach. Eng. Geol. 127, 54–64. https://doi.org/10.1016/j.enggeo.2012.01.001.

Alonso, J., Navarro, V., Calvo, B., Asensio, L., 2012b. Hydro-mechanical analysis of CO_2 storage in porous rocks using a critical state model. Int. J. Rock Mech. Mining Sci. 54, 19–26. https://doi.org/10.1016/j.ijrmms.2012.05.016.

Alonso, J., Moya, M., González, J., Asensio, L., Navarro, V., 2016. M4B: a tool for the multiphysics analysis of the deformational behaviour of soils and its interaction with building foundations. Comsol Conference Munich. 2016.

Alonso, J., Moya, M., Asensio, L., Navarro, V., Gómez, P., 2019. Disturbance of a natural hydrogeochemical system caused by the construction of a high-level radioactive waste facility: the case study of the central storage facility at Villar de Cañas, Spain. Adv. Wat. Res. 127, 264–279. https://doi.org/10.1016/j.advwatres.2019.03.020.

Appelo, C.A.J., 2015. Principles, caveats and improvements in databases for calculating hydrogeochemical reactions in saline waters from 0 to 200°C and 1 to 1000 atm. Appl. Geochem. 55, 62–71. https://doi.org/10.1016/j.apgeochem.2014.11.007.

Appelo, C.A.J., Parkhurst, D.L., Post, V.E.A., 2014. Equations for calculating hydrogeochemical reactions of minerals and gases such as CO_2 at high pressures and temperatures. Geochim. Comsochim. Ac. 125, 49–67. https://doi.org/10.1016/j.gca.2013.10.003.

Barton, A.F.M., Wilde, N.M., 1971. Dissolution rates of polycrystalline samples of gypsum and orthorhombic forms of calcium sulphate by a rotating disc method. Trans. Faraday Soc. 67 (583), 3590–3597.

Blount, C.W., Dickson, F.W., 1973. Gypsum-Anhydrite equilibria in Systems $CaSO_4$-H_2O and $CaCO_4$-NaCl-H_2O. Am. Mineral. 58, 323–331.

Cienfuegos, I., Mayor, J.C., Rueda, S., 2014. Informe resumen de integración para la caracterización del emplazamiento del ATC de Villar de Cañas (Cuenca). In: Technical Report: 042-IF-SU-0018, 12/2014, ENRESA (Madrid).

Colombani, J., 2008. Measurement of the pure dissolution rate constant of a mineral in water. Geochim. Cosmochim. Acta 72, 5634–5640. https://doi.org/10.1016/j.gca.2008.09.007.

Comsol, A.B., 2020. COMSOL Multiphysics Reference Guide, Version 5.6.

Cooper, A.H., Gutiérrez, F., 2013. Dealing with Gypsum Karst problems: hazards, environmental issues, and planning. In: Frumkin, A. (Ed.), Treatise on Geomorphology, Karst Geomorphology, vol. 6. Academic Press, San Diego, CA, pp. 451–462. https://doi.org/10.1016/B978-0-12-374739-6.00106-8.

Freyer, D., Voigt, W., 2003. Crystallization and phase stability of $CaSO_4$ and $CaSO_4$ -based salts. Monatsh. Chem. 134, 693–719. https://doi.org/10.1007/s00706-003-0590-3.
Gens, A., 2010. Soil–environment interactions in geotechnical engineering. Géotechnique. 60, 3–74. https://doi.org/10.1680/geot.9.P.109.
van Genuchten, M.T., 1980. A Closed-form equation for predicting the hydraulic conductivity of unsaturated soils. Soil Sci. Soc. Am. J. 44, 892–898.
Gobbert, M.K., Churchill, A., Wang, G., Seidman, T.I., 2009. COMSOL Multiphysics for efficient solution of a transient reaction-diffusion system with fast reaction. In: Rao, Y. (Ed.), Proceedings of the COMSOL Conference, Boston, 2009.
Gómez, P., Torres, E., Turrero, M.J., Peña, J., Garralón, A., Buil, B., Domínguez, R., Durán, J.M., Escribano, A., Sánchez, L., 2014. Estudio hidrogeoquímico del emplazamiento del Almacén Temporal Centralizado (ATC) en Villar de Cañas (Cuenca). In: Technical Report CIEMAT/DMA/2GO14/4/14, 12/2014, CIEMAT (Madrid).
Gumusoglu, M.C., Ulker, R., 1982. The investigation of the effect of gypsum on foundation design. Bull. Int. Assoc. Eng. Geol. 25, 99. https://doi.org/10.1007/BF02603199.
Gutiérrez, F., Parise, M., De Waele, J., Jourde, H., 2014. A review on natural and human-induced geohazards and impacts in karst. Earth Sci. Rev. 138, 61–88. https://doi.org/10.1016/j.earscirev.2014.08.002.
Hill, A.E., 1937. The transition temperature of gypsum to anhydrite. J Am. Chem. Soc. 59, 2242–2244. https://doi.org/10.1021/ja01290a039.
Huber, T., Pimentel, E., Anagnostou, G., 2015. Experimental investigations for the modelling of chemo-mechanical processes in anhydritic rock. Energy Procedia 76, 87–95.
James, A.N., 1992. Soluble Materials in Civil Engineering. Ellis Horwood Ltd., England, 433pp.
James, A.N., Lupton, A.R.R., 1978. Gypsum and anhydrite in foundations of hydraulic structures. Géotechnique. 28 (3), 249–272.
Janssen, H., Carmeliet, J., Hens, H., 2004. The influence of soil moisture transfer on building heat loss via the ground. Build. Environ. 39, 825–836. https://doi.org/10.1016/j.buildenv.2004.01.004.
Kaltreider, C., Krarti, M., McCartney, J., 2015. Heat transfer analysis of thermo-active foundations. Energy Build. 86, 492–501. https://doi.org/10.1016/j.enbuild.2014.09.063.
Klimchouk, A., 2000. Dissolution and conversions of gypsum and anhydrite. In: Klimchouk, A., Ford, D.C., Palmer, A.N., Dreybrodt, W. (Eds.), Speleogenesis. Evolution of Karst Aquifers. National Speleological Society, Huntsville, Alabama, pp. 160–168.
Kuttah, D., Sato, K., 2015. Review on the effect of gypsum content on soil behavior. Transport. Geotech. 4, 28–37. https://doi.org/10.1016/j.trgeo.2015.06.003.
Lasaga, A.C., 1998. Kinetic Theory in the Earth Sciences. Princeton University Press, Princeton, NJ.
Liu, S.T., Nancollas, G.H., 1971. The kinetics of dissolution of calcium sulfate dihydrate. J. Inorg. Nucl. Chem. 33, 2295–2311.
Martins, J.R.R.A., Hwang, J.T., 2013. Review and unification of methods for computing derivatives of multidisciplinary computational model. AIAA J. 51 (11), 2582–2599.
Meijer, J.A.M., 1983. Prevention of calcium sulfate scale deposition by a fluidized bed. Desalin. 47, 1–3.
Navarro, V., Asensio, L., Alonso, J., Yustres, A., Pintado, X., 2014a. Multiphysics implementation of advanced soil mechanics models. Comput. Geotech. 60, 20–28. https://doi.org/10.1016/j.compgeo.2014.03.012.
Navarro, V., Asensio, L., Yustres, A., Pintado, X., Alonso, J., 2014b. An elastoplastic model of bentonite free swelling. Eng. Geol. 181, 190–201. https://doi.org/10.1016/j.enggeo.2014.07.014.
Navarro, V., Asensio, L., De la Morena, G., Pintado, X., Yustres, A., 2015. Differentiated intra- and inter-aggregate water content models of mx-80 bentonite. Appl. Clay Sci. 118, 325–336. https://doi.org/10.1016/j.clay.2015.10.015.
Navarro, V., Asensio, L., Yustres, A., De la Morena, G., Pintado, X., 2016. Swelling and mechanical erosion of MX-80 bentonite: Pinhole test simulation. Eng. Geol. 202, 99–113. https://doi.org/10.1016/j.enggeo.2016.01.005.
Oldecop, L., Alonso, E., 2012. Modelling the degradation and swelling of clayey rocks bearing calcium-sulphate. Int. J. Rock Mech. Min. Sci. 54, 90–102. https://doi.org/10.1016/j.ijrmms.2012.05.027.
Ossorio, M., Van Driessche, A.E.S., Pérez, P., García-Ruiz, J.M., 2014. The gypsum –anhydrite paradox revisited. Chem. Geol. 386, 16–21. https://doi.org/10.1016/j.chemgeo.2014.07.026.
Paukštysa, B., Cooperb, A.H., Arustienec, J., 1999. Planning for gypsum geohazards in Lithuania and England. Eng. Geol. 52, 93–103. https://doi.org/10.1016/S0013-7952(98)00061-1.
Pintado, X., Lloret, A., Romero, E., 2009. Assessment of the use of the vapour equilibrium technique in controlled-suction tests. Canadian Geotechnical Journal 46 (4), 411–423.
Pollock, D.W., 1986. Simulation of fluid flow and energy transport processes associated with high-level radioactive waste disposal in unsaturated alluvium. Wat. Resour. Res. 22, 765–775. https://doi.org/10.1029/WR022i005p00765.
Posnjak, E., 1938. The system $CaSO_4$-H_2O. Am. J. Sci. Ser. 5 (35A), 247.
Ramon, A., Alonso, E.E., 2013. Heave of a railway bridge: modelling gypsum crystal growth. Géotechnique 63, 720–732. https://doi.org/10.1680/geot.2013.63.10.894.
Ramon, A., Alonso, E.E., Olivella, S., 2017. Hydro-chemo-mechanical modelling of tunnels in sulfated rocks. Géotechnique 67 (11), 968–982. https://doi.org/10.1680/jgeot.SiP17.P.252.
Rempel, A.R., Rempel, A.W., 2013. Rocks, clays, water, and salts: highly durable, infinitely rechargeable, eminently controllable thermal batteries for buildings. Geoscience 3, 63–101. https://doi.org/10.3390/geosciences3010063.
Rueda, S., Cienfuegos, I., Mayor, J.C., 2015. Estudio de caracterización del emplazamiento del ATC en Villar de Cañas (Cuenca) y de la zona de influencia de la instalación. In: Technical Report: 042-IF-TC-0008-Rev. 1, 05/2015, ENRESA (Madrid).
Sondon, M., 2016. Efectos osmóticos en el hinchamiento de las arcillas. Las Lutitas de Balanzas. Trabajo Final de Máster. Universidad Politécnica de Cataluña.
Van Driessche, A.E.S., Stawski, T.M., Kellermeier, M., 2019. Calcium sulfate precipitation pathways in natural and engineered environments. Chem. Geol. 530, 119274. https://doi.org/10.1016/j.chemgeo.2019.119274.
Villar, M.V., Iglesias, R.J., 2014. ATC: Caracterización básica y Termo-Hidro-Mecánica del sustrato. Anexo II al informe de síntesis de resultados. In: Informe de progreso 10/1/13 a 30/4/14. CIEMAT/DMA/2G214/3/14, CIEMAT (Madrid).
Wagner, R., Kühn Meyn, M.V., Pape, H., Vath, U., Clauser, C., 2005. Numerical simulation of pore space clogging in geothermal reservoirs by precipitation of anhydrite. Int. J. Rock Mech. Min. Sci. 42, 1070–1081.
Wang, Z., Wang, F., Ma, Z., Wang, X., Wu, X., 2016. Research of heat and moisture transfer influence on the characteristics of the ground heat pump exchangers in unsaturated soil. Energy Build. 130, 140–149. https://doi.org/10.1016/j.enbuild.2016.08.043.
Weitzmann, P., Kragh, L., Roots, P., Svendsen, S., 2005. Modelling floor heating systems using a validated two-dimensional ground-coupled numerical model. Build. Environ. 40, 153–163. https://doi.org/10.1016/j.buildenv.2004.07.010.
White, W.B., 1984. Rate processes: chemical kinetics and karst landform development. In: Landform Development, Groundwater as a Geomorphic Agent. Allen and Unwin, Boston, pp. 227–248.
Witkamp, G.J., van der Erden, J.P., van Rosmalen, G.M., 1990. Growth of gypsum. J. Cryst. Growth 102, 281–289.
Zanbak, K.C., Arthur, R.C., 1986. Geochemical and engineering aspects of anhydrite-gypsum phase transitions. Bull. Assoc. Eng. Geol. 23, 419–433. https://doi.org/10.2113/gseegeosci.xxiii.4.419.
Zdanovsky, A.B., 1956. Kinetics of Dissolution of Natural Salts in Conditions of Forced Convection. Goskhimizdat, Leningrad (219 p).
Zimmerman, R.W., Myer, L.R., Cook, N.G.W., 1994. Grain and void compression in fractured and porous rocks. Int. J. Rock. Mech. 31, 179–184. https://doi.org/10.1016/0148-9062(94)92809-6.